Anisotropic weak antilocalization in thin films of the Weyl semimetal TaAs

Ian A. Leahy,[1] Anthony D. Rice,[1] Chun-Sheng Jiang,[1] Goutam Paul,[1] Kirstin Alberi,[1,2] and Jocienne N. Nelson[1,*]

[1]*National Renewable Energy Laboratory, Golden, Colorado 80401, USA*

[2]*Renewable and Sustainable Energy Institute, National Renewable Energy Laboratory and University of Colorado, Boulder, Colorado 80301, USA*

(Received 7 May 2024; revised 17 July 2024; accepted 22 July 2024; published 22 August 2024)

Device applications of topological semimetals await the development of epitaxial films in the ultrathin limit. Weak antilocalization (WAL) has been extensively utilized in the understanding of surface states in topological insulators and shows promise for use in elucidating the properties of thin film topological semimetals. Here, we report insights from WAL in the surface state and interface transport properties of our recently synthesized single-crystal-like thin films of the Weyl semimetal TaAs(001) grown on GaAs(001). We observe robust, anisotropic WAL in the magnetoconductance from 2 to 20 K in films from 10 to 200 nm thick. We link the anisotropic WAL magnetoconductance to anisotropic mobility stemming from film topography. We conclude that WAL in the films likely originates from the antilocalization of topological surface states. The WAL magnetoconductance is impacted by the film thickness and topography, solidifying the useful role of WAL in the study of topological semimetal/semiconductor heterointerfaces.

DOI: 10.1103/PhysRevB.110.054206

I. INTRODUCTION

Maintaining low-resistance carrier transport in microelectronic devices is increasingly difficult as the dimensions of their electrical interconnects continue to shrink. Topological semimetals hold promise for addressing this challenge, as their two-dimensional (2D) Dirac and Fermi arc surface states can support high-mobility electron and hole conduction [1–3]. Among them, monopnictide Weyl semimetals (WSMs) are actively being explored for interconnects because of the large number of topological surface states [4–6]. Aspects of how their electronic structures impart control of electron transport and spin are also advantageous for optoelectronic, spintronic, and quantum computing applications [7–9]. In all cases, it is critical to understand the behavior of interfaces and how the presence of disorder inherent in thin heteroepitaxial films influences carrier transport through WSM surface and interface states. This was not possible until recent breakthroughs in thin film epitaxy [10,11].

Weak antilocalization (WAL) is an invaluable probe of the effects of disorder on surface states and can help us to understand the impact of disorder on carrier transport within ultrathin epitaxial WSMs. Weak localization (WL) and antilocalization have revealed important information about the surface states in topological insulators (TIs) [12–23]. WL is a quantum interference effect which decreases the conductivity of a system when backscattering probabilities are increased because of constructive interference of time-reversed loops composed of multiple electron-disorder scattering events [a schematic of this scattering is shown in the inset of Fig. 1(b)]. In the case of a system with strong spin-orbit coupling, this interference becomes destructive, resulting in an increase in the system's conductivity, known as WAL [13–15]. These interference effects require charge carriers to maintain phase coherence over multiple scattering events, typically referred to as the decoherence length l_ϕ, and are typically observed most readily at low temperatures. The application of a magnetic field introduces additional phase to carriers in these scattering loops, causing decoherence, suppressing the WL/WAL effects, and generating a characteristic field-dependent conductivity. Disorder is required to localize the relevant carriers and observe quantum corrections to the conductance. As such, the resulting magnetoconductance contains insight into localizing disorder length scales.

The interpretation of localization phenomena in TIs is fairly straightforward: the gapped bulk relegates the origin of localization magnetoconductance to the topological surface states. Systems are then manipulated with gating, doping, or growth conditions, and parameters from magnetoconductance fittings of localization effects are correlated to the number of topological conduction channels. Paired with decoherence lengths, information can be gleaned about the coupling of surface states and surface-to-bulk scattering. In thin WSMs, the interpretation of localization signatures is more complicated. Recently, WAL was observed in thin films of Dirac

*Present address: First Solar Inc., 1035 Walsh Avenue, Santa Clara, California 95050, USA; Contact author: jocienne.nelson@firstsolar.com

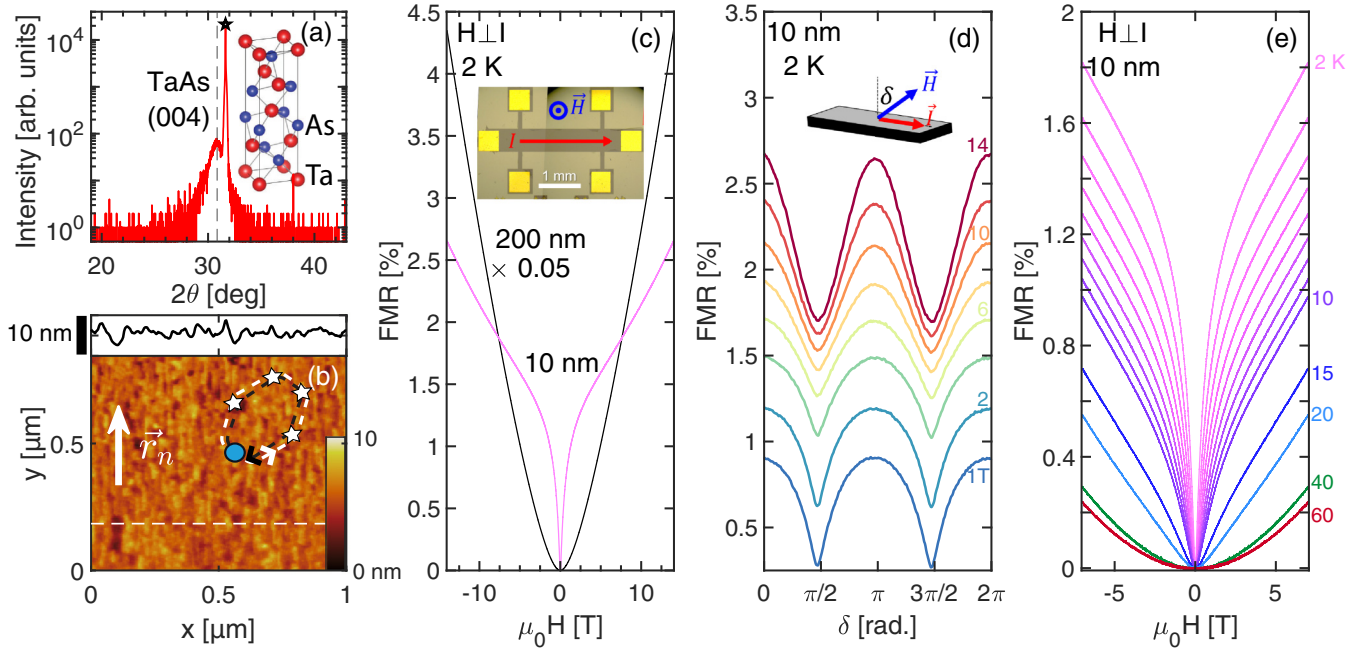

FIG. 1. (a) X-ray diffraction θ-2θ scan for a 10 nm TaAs (001)/GaAs (001) sample, indicative of single-phase growth. The star indicates the substrate peak. The inset shows the TaAs crystal structure. (b) Atomic force microscopy image on a film grown under similar conditions showing rodlike growth along $(\bar{1}10)$. The vector $\vec{r}_n$ defines the orientation of the rods. The inset axes show a line cut along the displayed white dashed line. A schematic illustration of an electron (blue circle) WAL scattering off of disorder (stars) around time-reversed paths (black and white lines) is overlaid, not to scale. (c) Fractional magnetoresistance for 10 nm (pink line) and 200 nm (black line) TaAs films vs applied field out of the plane, perpendicular to the current. The black data are scaled down 20 times for clarity. The sharp rise of the FMR of the 10 nm sample at low field originates from weak antilocalization. A large semiclassical FMR is visible in the 200 nm sample, and WAL is detectable at much smaller field scales (<0.02 T). The inset shows an optical image of a typical Hall bar. (d) Angle dependence of the FMR at several fixed magnetic fields at 2 K. Current is applied along $\vec{r}_n$. The inset shows the rotation direction. The observed angle-dependent signal is a combination of anisotropic magnetoresistance and weak antilocalization effects. While the AMR scales as $\sim\cos 2\delta$, a deviation occurs at low magnetic fields where the WAL effect distorts this dependence near $\delta = \pi/2$ and $3\pi/2$. (e) Fractional magnetoresistance vs magnetic field for the 10 nm sample at several temperatures. The WAL effect disappears above 20 K. The color map in (e) is after Crameri [27].

topological semimetals (TSMs) such as Cd_3As_2 [24–26], where the presence of topological and trivial surface states was inferred from the magnitude of the WAL magnetoconductance. The presence of WAL in ultrathin TSMs opens the possibility of studying this phenomenon to answer pressing questions about the robustness of topologically protected surface states in WSMs with regard to disorder and thickness.

In this paper, we derive insight into the role that disorder plays in transport through 2D surface states in thin heteroepitaxial TaAs WSM layers via the observation and analysis of WAL. The size of the observed WAL magnetoconductance depends on the orientation of the applied current relative to the film topography. The signature magnetoconductance is observed in samples ranging from 10 to 200 nm thick, likely indicative of the topological nature of the antilocalized state. While these films are highly defective and far from an ideal crystal, they represent material in a realistic device. It is important to understand how the desirable properties of WSMs, like their topological surface state transport, interact with significant disorder and transform in such conditions. Studies focusing on the robustness of these properties are essential to develop thin WSM devices that are compatible with industry-relevant processing flows such as sputtering.

II. RESULTS

Ultrathin films of TaAs were grown by molecular beam epitaxy (MBE) on GaAs(001) substrates miscut by 4° towards (111)A. A 500 nm GaAs buffer layer was deposited at 585 °C prior to TaAs growth. As_4 and Ta were codeposited at 640 °C with an As overpressure of 10–30:1 using a cracker source and an MBE Komponeten EBVV vertical electron beam evaporator, respectively. On select samples, the TaAs growth was followed by a GaAs capping layer to prevent surface oxidation. We have studied both uncapped and GaAs capped films and have observed minimal differences in their magnetoconductances. X-ray diffraction measurements were performed using a Rigaku Smartlab equipped with Cu $K\alpha$. Atomic force microscopy was performed in the tapping mode using a supersharp probe with a tip radius of 2–3 nm to ensure accurate topography. Six contact Hall bars were fabricated via standard photolithography, Ar ion etching, and electroplating of gold contacts. A Quantum Design physical property measurement system was used for temperature, field, and field-angle control. In our measurements the current lies in the crystallographic *ab* plane, and the magnetic field is rotated from along the *c* axis ($\delta = 0°$) to along the applied current ($\delta = 90°$) direction. More details on the film synthesis and characterization are given in Ref. [11].

Herein, we observe and analyze an anisotropic weak antilocalization signature in thin and ultrathin single-crystal-like Weyl semimetal TaAs films through a combination of MBE, magnetotransport, and atomic force microscopy (AFM). The ultrathin nature of some of our films enables the examination of isolated surface state transport. TaAs films were grown on conventional GaAs substrates, representing the types of disorder and interfaces that would be typical for WSM/semiconductor heterostructures. The TaAs films contain a high density of extended defects owing to the 16% lattice mismatch with GaAs. The film topographies feature the growth of $(\bar{1}10)$-oriented rods throughout. We find a large WAL signal that extends over a substantial field range ($\sim$1 T) and up to 20 K for numerous samples.

We begin with the characterization of a 10 nm thick TaAs sample. An x-ray diffraction θ-2θ scan of the film [Fig. 1(a)] confirms it has the bulk c-axis lattice parameter of TaAs [28]. The inset of Fig. 1(a) shows the TaAs crystal structure. Figure 1(b) shows AFM performed on a TaAs sample of similar thickness with an rms roughness of $R_q \approx 1$ nm. The topography consists of extended rodlike features that are approximately 100 nm long and 20–40 nm wide with 1–3 nm deep grooves between them. We define $\vec{r}_n$ as a vector which lies parallel to the long axis of the oriented rods in our films. These features are distinct from single-crystal-like bulk films [11] which have more squarelike morphologies. Although the film topographies evolve as a function of sample thickness, the ultrathin film AFM is consistent with other recent work on thin TaAs films [10,11].

Magnetotransport evidence supporting the existence of WAL in TaAs is shown in Figs. 1(c)–1(e). The fractional magnetoresistance (FMR) is defined as

$$\mathrm{FMR} \equiv \frac{R_S(H) - R_S(0\mathrm{T})}{R_S(0\mathrm{T})} \times 100\%, \tag{1}$$

where $R_S(H)$ is the sheet resistance as a function of applied field at fixed temperature. Figure 1(c) shows the FMR for perpendicular applied fields up to 14 T at 2 K. The magnitude of the FMR reaches values of a few percent at 14 T. These values are much smaller than those observed in bulk samples owing to the reduced carrier mobility stemming from defects in the film in combination with the unintentional hole doping [11]. A marked difference is visible in the functional dependence of the FMR for the 10 and 200 nm samples. The sharp low-field rise in the FMR for the 10 nm film is a characteristic signature of WAL. The obvious WAL cusp is replaced with a semiclassical FMR in the 200 nm film, although WAL is still observable at reduced field scales [Fig. 3(c)].

To further verify the WAL effect, we measure the applied field-angle dependence of the FMR at 2 K in the 10 nm sample as the magnetic field is rotated from perpendicular to the plane of the film ($\delta = 0$) into the current direction ($\delta = \pi/2$), shown in Fig. 1(d). At high magnetic fields, the FMR follows a $\cos 2\delta$ dependence, typical of anisotropic magnetoresistance. At lower fields, the measured FMR sharpens when the field is parallel or antiparallel to the current direction ($\delta = \pi/2,\ 3\pi/2$). This is due to a rapid reduction in the WAL contribution as the field tilts into the plane and is routinely observed in systems with WAL [20,23].

TABLE I. Summary of 2 K electrical transport and WAL properties. Carrier density and sheet mobility as a function of temperature are given in Fig. S3 in the Supplemental Material.

Sample	n_{2D} (10^{14} cm^{-2})	μ (cm^2/V s)
$I \perp \vec{r}_n$	9.35	10.6
$I \parallel \vec{r}_n$	9.24	24.4

The temperature dependence of the FMR ($H \perp I$) for the 10 nm film is shown in Fig. 1(e) up to 60 K. With increasing temperature, the low-field WAL cusp gradually broadens and decreases in magnitude before disappearing above 20 K. In addition, the magnetic field scaling of the high-field FMR changes from sublinear with field at 2 K to nearly quadratic at 40 K.

To gain more insight into the WAL in our TaAs films, we compare the low-field dependence of the magnetoconductance $[\Delta G = 1/R_s(H) - 1/R_s(0\mathrm{T})]$ in two $\sim$11 nm samples with $I \perp \vec{r}_n$ [Fig. 2(a)] and $I \parallel \vec{r}_n$ [Fig. 2(b)]. The vector $\vec{r}_n$ is oriented along the rodlike growth features. We highlight that the samples in Figs. 2(a) and 2(b) are prepared from the same film in perpendicular orientations. The orientations of the rods relative to the direction of the applied current were confirmed on the same samples with AFM [Figs. 2(d) and 2(e)]. Most clearly, we observe an anisotropy in the measured WAL magnetoconductance, with the $I \parallel \vec{r}_n$ orientation exhibiting a ΔG roughly 2 times larger than that in the $I \perp \vec{r}_n$ case. Typically, the magnetoconductance originating from 2D localization or WAL with spin-orbit coupling can be described by the Hikami-Larkin-Nagaoka (HLN) formula [13,20,23]:

$$\Delta G_{\mathrm{HLN}} = \frac{\alpha e^2}{\pi h}\left[\psi\left(\frac{1}{2} + \frac{H_\phi}{|H\cos\delta|}\right) - \ln\left(\frac{H_\phi}{|H\cos\delta|}\right)\right], \tag{2}$$

where ψ is the digamma function, α is a measure of the number of conduction channels, and $H_\phi = \hbar/(4el_\phi^2)$, where l_ϕ is the phase coherence length. We note that the use of this simple HLN equation with no additional spin-orbit coupling terms is justified as we do not observe a crossover to WL behavior as a function of field in any temperature for any sample reported here [29]. In the case of a material with an anisotropic conductivity, the HLN equation is modified [30–32]. Due to the variation in the number of grain boundaries encountered for $I \perp \vec{r}_n$ and $I \parallel \vec{r}_n$, we observe a substantial difference in the mobilities in perpendicular directions (Table I). Our films are unintentionally hole doped from defects, consistent with literature works on thin film TaAs, exhibiting 2 orders of magnitude higher hole concentrations than bulk single crystals [11,33,34]. Additionally, the measured mobilities are similarly reduced (2 orders of magnitude) compared to the bulk, stemming from the grain boundary and defect scattering. For the sample orientations presented here, we rewrite the HLN equation including the conductivity anisotropy as

$$\Delta G_{\parallel,\perp} = A_{\parallel,\perp}\Delta G_{\mathrm{HLN}}, \tag{3}$$

where $A_{\parallel,\perp} \equiv n_{\parallel,\perp}\mu_{\parallel,\perp}/\sqrt{n_\parallel\mu_\parallel n_\perp\mu_\perp}$ and $\mu_{\parallel,\perp}$ and $n_{\parallel,\perp}$ represent the mobility and carrier densities measured with the applied current parallel or perpendicular to $\vec{r}_n$. In Fig. 2(c),

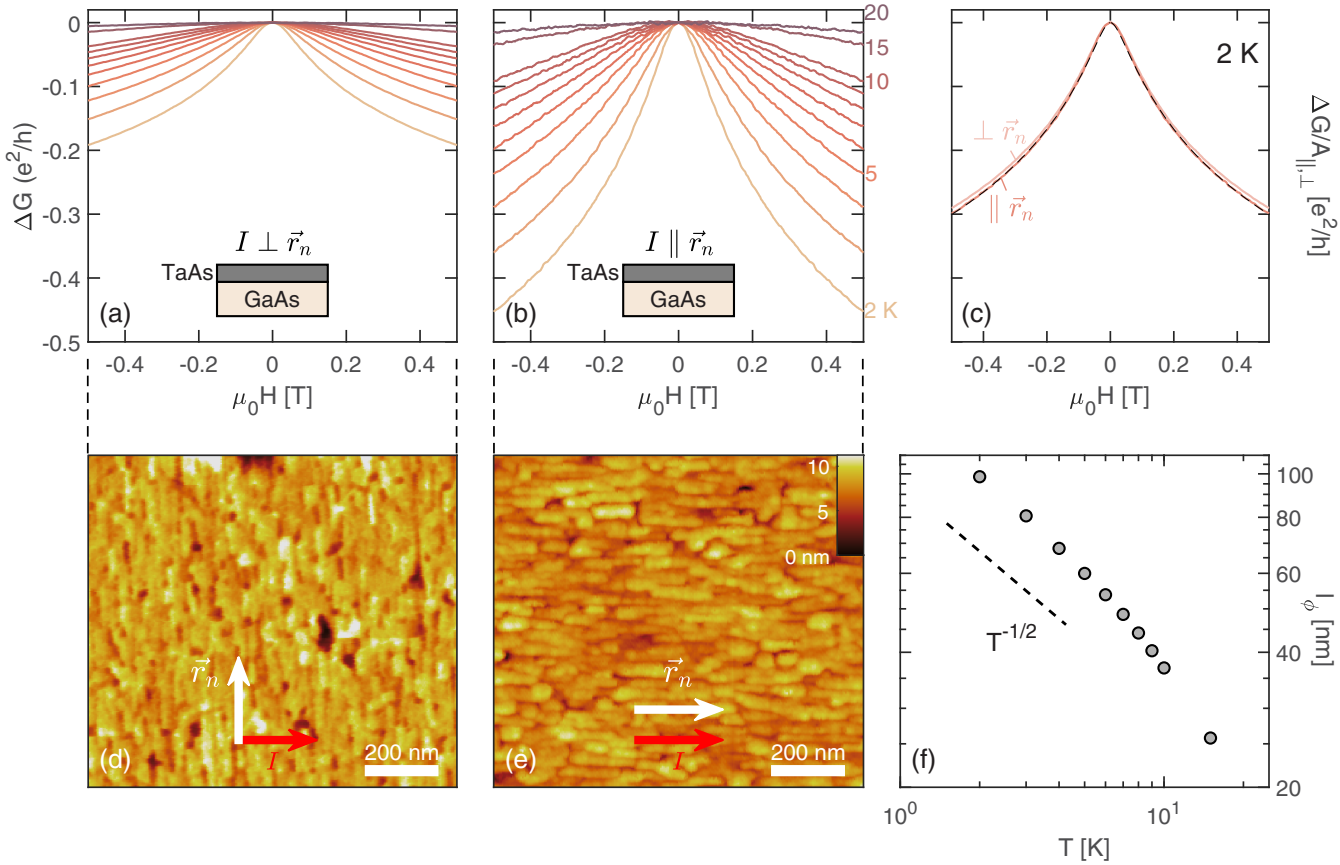

FIG. 2. The perpendicular magnetic field dependence of the sheet conductance $[\Delta G = 1/R_S(H) - 1/R_S(0)]$ at several fixed temperatures for two samples made from a single TaAs film with (a) $I \perp \vec{r}_n$ and (b) $I \parallel \vec{r}_n$, where $\vec{r}_n$ points along the primary growth direction of the rodlike features observed in our films. (c) Sheet conductance normalized by $A_{\parallel,\perp}$ for the 2 K data in (a) and (b). The normalization collapses the data in orthogonal directions. The dashed black line is a fit of the scaled $I \parallel \vec{r}_n$ data to Eq. (3). AFM images for the corresponding Hall bars with (d) $I \perp \vec{r}_n$ and (e) $I \parallel \vec{r}_n$. (f) The decoherence length l_ϕ extracted from the anisotropic HLN analysis. The dashed line represents the $T^{-1/2}$ scaling indicative of electron-electron-mediated decoherence processes. Color maps in (a)–(c) are after Crameri [27].

we show the effect of removing the mobility anisotropy from the WAL magnetoconductance by plotting $\Delta G/A_{\parallel,\perp}$ at 2 K for the samples with orthogonal currents. Scaling by $A_{\parallel,\perp}$ collapses the magnetoconductance for these samples, verifying that the anisotropy in the WAL originates from the anisotropic conductivity.

Scaling all traces using $A_{\parallel,\perp}$, we fit the WAL magnetoconductance at different fixed temperatures (see the Supplemental Material (SM), Fig. S1 [35]). Figure 2(f) shows the extracted l_ϕ, which reaches a 2 K value of 99 nm and decreases monotonically with increasing temperature. We find a value of $\alpha = -0.6$ at 2 K, close to the value expected for a single conduction channel ($\alpha = -0.5$). The temperature dependence of l_ϕ reveals details about the mechanism responsible for phase decoherence in our films. Below 10 K, the decoherence length scales as $T^{-0.55}$, consistent with the scaling expected for decoherence caused by electron-electron interactions in two dimensions ($T^{-0.5}$) [22,36]. We corroborate this decoherence mechanism in the SM by examining the temperature dependence of the sheet resistance (SM, Fig. S2).

Finally, we turn our attention to the measurement of the WAL effect in TaAs samples of various thicknesses. Figure 3 shows visible WAL for $I \parallel \vec{r}_n$ for samples up to 200 nm thick. We highlight the field scales of the WAL effect shrink with growing thickness. At 200 nm, the WAL is visible only below 0.02 T, signifying that the decoherence length increases significantly in thicker films. As the films grow

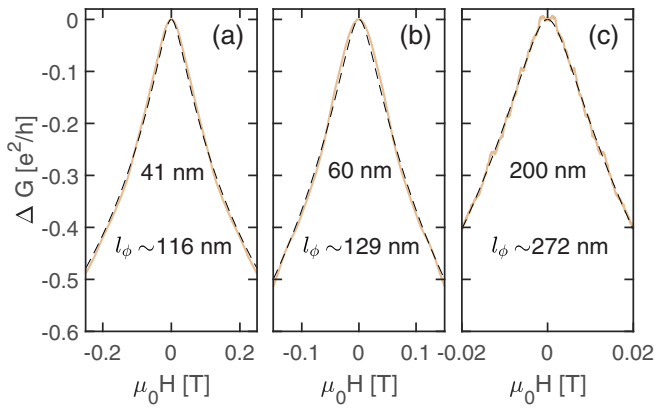

FIG. 3. Field perpendicular WAL magnetoconductance for (a) 41, (b) 60, and (c) 200 nm films. A single band background is subtracted in the 200 nm thick data (SM, Fig. S4). Dashed lines indicate fits to the HLN equation. As the thickness increases, the field range where the WAL is visible decreases, corresponding to an increasing decoherence length.

thicker, semiclassical multiband contributions make the WAL more difficult to measure. For the 200 nm film, we subtract a semiclassical single-band contribution from the raw magnetoconductance (SM, Fig. S4). Additionally, the overall anisotropy is reduced as the rodlike features visible in the ultrathin films coalesce and homogenize into squarelike grains with thicker film growth [11]. We have measured that the WAL anisotropy remains in films up to 60 nm thick (SM, Fig. S5), although the scaling by $A_{\parallel,\perp}$ collapses the $I \parallel \vec{r}_n$ and $I \perp \vec{r}_n$ datasets only to within ≈20% owing to the increasing dimensionality, bulk contribution, and changing topographical anisotropy. Dashed lines in Fig. 3 represent fits to Eq. (2), showing good agreement with the HLN model, even for the 200 nm thick film. We find values of $\alpha = -1.17, -1.50$, and -1.82 for the 41, 61, and 200 nm films, respectively. These values are overestimates because of the growing semiclassical magnetoconductance, three-dimensionality, and difficulty with anisotropy scaling in thicker films. The decoherence length increases as the films get thicker, consistent with the regularization of the rodlike growth into squarelike grains (SM, Fig. S6).

III. DISCUSSION

We start our discussion by considering WAL observations in TaAs. WAL has been observed in bulk TaAs and was found to be consistent with theoretical predictions for three-dimensional (3D) WAL in a WSM [37,38]. We find that the theoretical expressions given for the 3D WSM WAL in bulk TaAs are unable to reproduce our experimental data more faithfully than the simple (anisotropic) 2D HLN model, even in the 200 nm, bulklike films. Additionally, spin-orbit terms are excluded from the HLN model because no significant crossover from WAL to WL as a function of field is observed in any sample at any temperature (Note 7 in the Supplemental Material Ref. [35]). Thus, we focus on localization within the HLN model. In TaAs, what states are being weakly antilocalized and why?

Generally, states with nontrivial spin-momentum locking can become weakly antilocalized. For TaAs the topological surface states are the obvious candidate, although we must consider other possibilities such as confined bulk states as well as trivial surface states. If confined bulk states were the origin of the WAL effect, we would expect the WAL effect to change and likely vanish, as the confinement is wiped away with increasing thickness—no such effect is observed. In TaAs, it has been shown that the spin texture of surface states can be used to gain information about the trivial or topological nature of a particular surface state: the topological surface states have nontrivial spin-momentum-locked spin texture, while the trivial surface states do not [39]. Rashba spin-orbit coupling at the GaAs/TaAs interface could introduce some spin texture to trivial surface states and cause a twisting of the spin texture of the topological surface states [40], although this effect is likely secondary compared to the existing spin texture of the topological surface states. Thus, it is most likely that the topological surface states are the channels experiencing antilocalization.

For our 11 nm thick films, $\alpha = -0.6$ is similar to the theoretical value of $\alpha = -0.5$ expected for a single conduction channel. Deviations from the expected value could stem from several effects, such as bulk-surface coupling and coupling of surface states on opposite sides of the film. In the 11 nm films, this deviation is likely some degree of coupling between states on the top and bottom surfaces. As the films get thicker, the coupling reduces. Indeed, the WAL magnetoconductance for thicker films has $\alpha \leqslant -1$, consistent with two conduction channels or a decoupling of states on the top and bottom surfaces of the films.

In summary, we have analyzed weak antilocalization effects in WSM TaAs films grown via MBE to understand the role of disorder on electrical transport. We observed an anisotropic WAL response that depends on the orientation of the applied current relative to the film topography. This anisotropic WAL magnetoconductance was found to be consistent with the anisotropic 2D HLN model. Signatures of anisotropic WAL were measured in films up to 60 nm thick, and WAL was observed in samples up to 200 nm thick. We discussed possible origins of the WAL in TaAs, concluding that antilocalized topological surface states are the probable culprit. The number of conduction channels changes as the films grow thicker, likely consistent with the decoupling of topological surface states on the top and bottom film surfaces. In moving toward heterostructures for device applications, we can infer from these results that film morphology will likely play a role in transport through topological and trivial states and must be controlled to the extent possible. Further, we highlight that WAL can play a role in understanding the effects of different WSM/semiconductor heterostructures on topological surface states.

The data that support the findings of this study are available from the corresponding author upon reasonable request.

ACKNOWLEDGMENTS

This work was authored in part by the National Renewable Energy Laboratory, operated by the Alliance for Sustainable Energy, LLC, for the U.S. Department of Energy (DOE) under Contract No. DE-AC36-08GO28308. Funding to perform TaAs epitaxy and basic structural characterization was supported through an NREL Director's Fellowship. Funding for the investigation of the magnetotransport and WAL effects was supported by the U.S. Department of Energy, Office of Science, Basic Energy Sciences, Division of Materials Sciences and Engineering, Physical Behavior of Materials Program.

The views expressed in the article do not necessarily represent the views of the DOE or the U.S. Government. The U.S. Government retains and the publisher, by accepting the article for publication, acknowledges that the U.S. Government retains a nonexclusive, paid-up, irrevocable, worldwide license to publish or reproduce the published form of this work, or allow others to do so, for U.S. Government purposes.

J.N.N. conceived the project. I.A.L., J.N.N., and K.A. prepared the manuscript. J.N.N. and A.D.R. grew the samples and performed structural characterization. J.N.N. and I.A.L. performed the electrical transport characterization and analysis. C.-S.J. and G.P. performed the AFM measurements.

[1] B. Yan and C. Felser, Topological materials: Weyl semimetals, Annu. Rev. Condens. Matter Phys. **8**, 337 (2017).

[2] S. Kumar, Y.-H. Tu, S. Luo, N. A. Lanzillo, T.-R. Chang, G. Liang, R. Sundararaman, H. Lin, and C.-T. Chen, Surface-dominated conductance scaling in Weyl semimetal NbAs, npj Comput. Mater. **10**, 84 (2024).

[3] C. Zhang, Z. Ni, J. Zhang, X. Yuan, Y. Liu, Y. Zou, Z. Liao, Y. Du, A. Narayan, H. Zhang, T. Gu, X. Zhu, L. Pi, S. Sanvito, X. Han, J. Zou, Y. Shi, X. Wan, S. Y. Savrasov, and F. Xiu, Ultrahigh conductivity in Weyl semimetal NbAs nanobelts, Nat. Mater. **18**, 482 (2019).

[4] N. P. Armitage, E. J. Mele, and A. Vishwanath, Weyl and Dirac semimetals in three-dimensional solids, Rev. Mod. Phys. **90**, 015001 (2018).

[5] C.-T. Chen, U. Bajpai, N. A. Lanzillo, C.-H. Hsu, H. Lin, and G. Liang, Topological semimetals for scaled back-end-of-l interconnect beyond Cu, in *2020 IEEE International Electron Devices Meeting (IEDM)* (IEEE, Piscataway, NJ, 2020), pp. 32.4.1–32.4.4.

[6] S.-W. Lien, I. Garate, U. Bajpai, C.-Y. Huang, C.-H. Hsu, Y.-H. Tu, N. A. Lanzillo, A. Bansil, T.-R. Chang, G. Liang, H. Lin, and C.-T. Chen, Unconventional resistivity scaling in topological semimetal CoSi, npj Quantum Mater. **8**, 3 (2023).

[7] J. Liu, F. Xia, D. Xiao, F. J. García De Abajo, and D. Sun, Semimetals for high-performance photodetection, Nat. Mater. **19**, 830 (2020).

[8] Q. Lv, P.-H. Fu, X.-L. Yu, J.-F. Liu, and J. Wu, Electrically controlled spin polarized current in Dirac semimetals, Sci. Rep. **11**, 21509 (2021).

[9] A. A. Burkov, Topological semimetals, Nat. Mater. **15**, 1145 (2016).

[10] J. Sadowski, J. Z. Domagała, W. Zajkowska, S. Kret, B. Seredyński, M. Gryglas-Borysiewicz, Z. Ogorzałek, R. Bożek, and W. Pacuski, Structural properties of TaAs Weyl semimetal thin films grown by molecular beam epitaxy on GaAs(001) substrates, Cryst. Growth Des. **22**, 6039 (2022).

[11] J. N. Nelson, A. D. Rice, R. Kurleto, A. Shackelford, Z. Sierzega, P. Hao, B. S. Berggren, C.-S. Jiang, A. G. Norman, M. E. Holtz, J. S. Mangum, I. A. Leahy, K. N. Heinselman, H. Ness, M. Van Schilfgaarde, D. S. Dessau, and K. Alberi, Thin-film TaAs: Developing a platform for Weyl semimetal devices, Matter **6**, 2886 (2023).

[12] B. L. Altshuler, D. Khmel'nitzkii, A. I. Larkin, and P. A. Lee, Magnetoresistance and Hall effect in a disordered two-dimensional electron gas, Phys. Rev. B **22**, 5142 (1980).

[13] S. Hikami, A. I. Larkin, and Y. Nagaoka, Spin-orbit interaction and magnetoresistance in the two dimensional random system, Prog. Theor. Phys. **63**, 707 (1980).

[14] S. Sangiao, N. Marcano, J. Fan, L. Morellón, M. R. Ibarra, and J. M. D. Teresa, Quantitative analysis of the weak anti-localization effect in ultrathin bismuth films, Europhys. Lett. **95**, 37002 (2011).

[15] Y. S. Kim, M. Brahlek, N. Bansal, E. Edrey, G. A. Kapilevich, K. Iida, M. Tanimura, Y. Horibe, S.-W. Cheong, and S. Oh, Thickness-dependent bulk properties and weak antilocalization effect in topological insulator Bi_2Se_3, Phys. Rev. B **84**, 073109 (2011).

[16] L. Bao, L. He, N. Meyer, X. Kou, P. Zhang, Z.-g. Chen, A. V. Fedorov, J. Zou, T. M. Riedemann, T. A. Lograsso, K. L. Wang, G. Tuttle, and F. Xiu, Weak anti-localization and quantum oscillations of surface states in topological insulator Bi_2Se_2Te, Sci. Rep. **2**, 726 (2012).

[17] Y. Takagaki, B. Jenichen, U. Jahn, M. Ramsteiner, and K.-J. Friedland, Weak antilocalization and electron-electron interaction effects in Cu-doped Bi_2Se_3 films, Phys. Rev. B **85**, 115314 (2012).

[18] M. Lang, L. He, X. Kou, P. Upadhyaya, Y. Fan, H. Chu, Y. Jiang, J. H. Bardarson, W. Jiang, E. S. Choi, Y. Wang, N.-C. Yeh, J. Moore, and K. L. Wang, Competing weak localization and weak antilocalization in ultrathin topological insulators, Nano Lett. **13**, 48 (2013).

[19] H.-Z. Lu and S.-Q. Shen, Weak localization and weak anti-localization in topological insulators, Proc. SPIE **9167**, 91672E (2014).

[20] H. Li, H.-W. Wang, Y. Li, H. Zhang, S. Zhang, X.-C. Pan, B. Jia, F. Song, and J. Wang, Quantitative analysis of weak antilocalization effect of topological surface states in topological insulator $BiSbTeSe_2$, Nano Lett. **19**, 2450 (2019).

[21] S. Gupta, R. Sachan, and J. Narayan, Evidence of weak antilocalization in epitaxial TiN thin films, J. Magn. Magn. Mater. **498**, 166094 (2020).

[22] R. Gracia-Abad, S. Sangiao, C. Bigi, S. Kumar Chaluvadi, P. Orgiani, and J. M. De Teresa, Omnipresence of weak antilocalization (WAL) in Bi_2Se_3 thin films: A review on its origin, Nanomaterials **11**, 1077 (2021).

[23] S. Sasmal, J. Mukherjee, D. Suri, and K. V. Raman, In-depth analysis of anisotropic magnetoconductance in Bi_2Se_3 thin films with electron–electron interaction corrections, J. Phys.: Condens. Matter **33**, 465601 (2021).

[24] B. Zhao, P. Cheng, H. Pan, S. Zhang, B. Wang, G. Wang, F. Xiu, and F. Song, Weak antilocalization in Cd_3As_2 thin films, Sci. Rep. **6**, 22377 (2016).

[25] J. Hellerstedt, M. T. Edmonds, N. Ramakrishnan, C. Liu, B. Weber, A. Tadich, K. M. O'Donnell, S. Adam, and M. S. Fuhrer, Electronic properties of high-quality epitaxial topological Dirac semimetal thin films, Nano Lett. **16**, 3210 (2016).

[26] W. Yu, D. X. Rademacher, N. R. Valdez, M. A. Rodriguez, T. M. Nenoff, and W. Pan, Evidence of decoupling of surface and bulk states in Dirac semimetal Cd_3As_2, Nanotechnology **33**, 415002 (2022).

[27] F. Crameri, "Scientific colour maps (8.0.1) (2023)" Zenodo, doi:10.5281/zenodo.8409685.

[28] J. J. Murray, J. B. Taylor, L. D. Calvert, Y. Wang, E. J. Gabe, and J. G. Despault, Phase relationships and thermodynamics of refractory metal pnictides: The metal-rich tantalum arsenides, J. Less-Common Met. **46**, 311 (1976).

[29] Y. J. Zhang, W. Shi, J. T. Ye, R. Suzuki, and Y. Iwasa, Robustly protected carrier spin relaxation in electrostatically doped transition-metal dichalcogenides, Phys. Rev. B **95**, 205302 (2017).

[30] O. Bierwagen, C. Walther, W. T. Masselink, and K.-J. Friedland, Weak localization in laterally coupled quantum wires, Phys. Rev. B **67**, 195331 (2003).

[31] C. W. J. Beenakker and H. van Houten, Quantum transport in semiconductor nanostructures, Solid State Phys. **44**, 1 (1991).

[32] P. A. Lee and T. V. Ramakrishnan, Disordered electronic systems, Rev. Mod. Phys. **57**, 287 (1985).

[33] R. Sankar, G. Peramaiyan, I. P. Muthuselvam, S. Xu, M. Z. Hasan, and F. C. Chou, Crystal growth and transport properties of Weyl semimetal TaAs, J. Phys.: Condens. Matter **30**, 015803 (2018).

[34] M. Naumann, F. Arnold, M. D. Bachmann, K. A. Modic, P. J. W. Moll, V. Süß, M. Schmidt, and E. Hassinger, Orbital effect and weak localization in the longitudinal magnetoresistance of Weyl semimetals NbP, NbAs, TaP, and TaAs, Phys. Rev. Mater. **4**, 034201 (2020).

[35] See Supplemental Material at http://link.aps.org/supplemental/10.1103/PhysRevB.110.054206 for additional discussion and information regarding (1) anisotropic WAL scaling, (2) the temperature dependence of the sheet resistance, (3) the temperature dependence of the sheet carrier density and mobility, (4) single-band background subtraction for the 200 nm thick film, (5) WAL anisotropy in additional samples to 60 nm thick, (6) AFM in additional samples up to 200 nm thick, (7) WAL vs WL in TaAs and extended magnetoconductance to 7 T, and (8) analyzing multichannel WAL with anisotropic decoherence lengths, with Refs. [12,17,21,32,36,41–50] therein.

[36] B. L. Altshuler, A. G. Aronov, and D. E. Khmelnitsky, Effects of electron-electron collisions with small energy transfers on quantum localisation, J. Phys. C **15**, 7367 (1982).

[37] C. L. Zhang, S. Y. Xu, I. Belopolski, Z. Yuan, Z. Lin, B. Tong, G. Bian, N. Alidoust, C. C. Lee, S. M. Huang, T. R. Chang, G. Chang, C. H. Hsu, H. T. Jeng, M. Neupane, D. S. Sanchez, H. Zheng, J. Wang, H. Lin, C. Zhang *et al.*, Signatures of the Adler-Bell-Jackiw chiral anomaly in a Weyl fermion semimetal, Nat. Commun. **7**, 10735 (2016).

[38] H.-Z. Lu and S.-Q. Shen, Weak antilocalization and localization in disordered and interacting Weyl semimetals, Phys. Rev. B **92**, 035203 (2015).

[39] Y. Sun, S.-C. Wu, and B. Yan, Topological surface states and Fermi arcs of the noncentrosymmetric Weyl semimetals TaAs, TaP, NbAs, and NbP, Phys. Rev. B **92**, 115428 (2015).

[40] Y. Baba, F. Domínguez-Adame, G. Platero, and R. A. Molina, Rashba coupling and spin switching through surface states of Dirac semimetals, New J. Phys. **23**, 023008 (2021).

[41] J. Kondo, Resistance minimum in dilute magnetic alloys, Prog. Theor. Phys. **32**, 37 (1964).

[42] M. M. A. Yajadda, K.-H. Müller, and K. Ostrikov, Effect of Coulomb blockade, gold resistance, and thermal expansion on the electrical resistance of ultrathin gold films, Phys. Rev. B **84**, 235431 (2011).

[43] B. L. Al'tshuler and A. G. Aronov, Contribution to the theory of disordered metals in strongly doped semiconductors, Zh. Eksp. Teor. Fiz. **77**, 2028 (1979) [Sov. Phys. JETP **50**, 968 (1979)].

[44] J. Wang, A. M. DaSilva, C.-Z. Chang, K. He, J. K. Jain, N. Samarth, X.-C. Ma, Q.-K. Xue, and M. H. W. Chan, Evidence for electron-electron interaction in topological insulator thin films, Phys. Rev. B **83**, 245438 (2011).

[45] L. Balcells, J. Fontcuberta, B. Martínez, and X. Obradors, High-field magnetoresistance at interfaces in manganese perovskites, Phys. Rev. B **58**, R14697 (1998).

[46] M. A. Blachly and N. Giordano, Kondo effect in quasi-two dimensions: The role of disorder, Europhys. Lett. **27**, 687 (1994).

[47] Z. Xie, X. Wei, S. Cao, Y. Zhang, S. Yan, G. D. Gu, Q. Li, and J.-H. Chen, Electron-electron interactions and weak antilocalization in few-layer $ZrTe_5$ devices, Phys. Rev. B **103**, 155408 (2021).

[48] B. J. Ramshaw, K. A. Modic, A. Shekhter, Y. Zhang, E.-A. Kim, P. J. W. Moll, M. D. Bachmann, M. K. Chan, J. B. Betts, F. Balakirev, A. Migliori, N. J. Ghimire, E. D. Bauer, F. Ronning, and R. D. McDonald, Quantum limit transport and destruction of the Weyl nodes in TaAs, Nat. Commun. **9**, 2217 (2018).

[49] J. Ziman, *Electrons and Phonons: The Theory of Transport Phenomena in Solids* (Oxford University Press, Oxford, 2001).

[50] L. Liu, Z.-Q. Wang, C.-E. Hu, Y. Cheng, and G.-F. Ji, Comparative study on structural, elastic, dynamical, and thermodynamic properties of Weyl semimetals MX (M = Ta or Nb; X = As or P), Solid State Commun. **263**, 10 (2017).